J Solid State Electrochem (2012) 16:1585–1593
DOI 10.1007/s10008-011-1559-5

ORIGINAL PAPER

Paper like free-standing hybrid single-walled carbon nanotubes air electrodes for zinc–air batteries

Nutan Gupta · Tingji Toh · Mak Wai Fatt · Subodh Mhaisalkar · Madhavi Srinivasan

Received: 21 June 2011 / Revised: 12 September 2011 / Accepted: 20 September 2011 / Published online: 14 October 2011

Abstract Flexible electrode architectures based on non-functionalized (P2) and functionalized (P3) single-walled carbon nanotubes (SWNTs) were fabricated via a simple vacuum filtration process. A hybrid layer of various compositions of P2- and P3-SWNTs forms free-standing membranes (~80 μm in thickness), and their electrochemical performance was evaluated as an air electrode $AE_{P2/P3}$ in zinc–air batteries. Such bifunctionalized air electrodes showed uniform surface morphology with interconnected micron-sized porous structure with high porosity (~70%). The N_2 adsorption isotherms at 77 K are of type IV with BET-specific surface areas of $AE_{(60/40)}$ and $AE_{(80/20)}$ to be 130.54 and 158.76 $m^2\ g^{-1}$, respectively, thus facilitates high active surface area for active oxygen reduction/evolution reactions. BJH pore size distribution of $AE_{(60/40)}$ and $AE_{(80/20)}$ shows maximum pores with diameter <15 nm. The zigzag interlaying of the SWNTs imparts mechanical stability and flexibility in zinc–air batteries. Zinc–air batteries with optimized compositions of P2- and P3-SWNTs in air electrode $AE_{(60/40)}$ had ionic conductivity ~1×10^{-2} S cm^{-1} and delivered higher discharge capacity ~300 mAh g^{-1} as compared to $AE_{(80/20)}$ composition. The unique properties of $AE_{(P2/P3)}$ studied in this work would enable flexible air electrode architectures in future metal–air batteries.

N. Gupta · T. Toh · M. W. Fatt · S. Mhaisalkar · M. Srinivasan (✉)
School of Materials Science and Engineering,
Nanyang Technological University,
Block N4.1, 50 Nanyang Avenue,
Singapore 639798, Singapore
e-mail: madhavi@ntu.edu.sg

N. Gupta · T. Toh · M. W. Fatt · S. Mhaisalkar · M. Srinivasan
Energy Research Institute @ NTU (ERI@N),
Research Techno Plaza, 50 Nanyang Drive,
Singapore 637553, Singapore

Keywords Zinc–air batteries · Carbon nanotubes · Air electrode · Porosity · Discharge capacity

Introduction

Increasingly sophisticated energy storage demands from consumer electronics and electric vehicles require high-energy storage platform that is low-cost, safe, and durable. Recently, zinc–air batteries have gained more attention due to its high practical specific energy (~350 Wh kg^{-1}), low-cost steady performance, and environmental benign as compared to lithium ion batteries (~180 Wh kg^{-1}) [1–3]. In zinc–air batteries, only the active negative electrode (zinc) is stored in the battery while the reactant for the positive electrode (O_2/air) is drawn from the atmosphere using air electrode (AE) during discharge which leads to its high theoretical energy density (1,370 Wh kg^{-1}) distinctly higher than Li-ion batteries [4]. One of the key problems to exploit this theoretical high energy density of zinc–air batteries is the lack of suitable AE or gas diffusion electrodes whose design/formulation has been an important factor in determining the discharge capacity and specific energy of zinc–air batteries [5]. AE design in zinc–air button cells usually includes a catalyst layer, metallic mesh screen, hydrophobic membrane and diffusion membrane, and air distribution layer. Such multilayered AEs are fabricated by pressing thick carbon powder on both sides of a metallic nickel mesh current collector (and support) along with a binder for mechanical stability of the carbon layers. In addition to carbon, AE consists of a hydrophobic additive such as polytetrafluoroethylene (PTFE) on the air facing side to avoid flooding of the pores with electrolyte and a catalyst layer to promote oxygen reduction reaction [6–9]. Fabrication of such AE demonstrates a complex

multilayer architecture in order to establish a three-phase boundary between the gaseous materials (O_2/air), the liquid electrolyte, and the solid current collector [10, 11].

Single-walled carbon nanotubes (SWNTs) can potentially replace the complex multilayer carbon-based AE architecture because SWNTs form very thin and freestanding entangled networks (so-called "bucky papers") which are not only highly conducting and porous but also mechanically robust. Hence, neither current collectors nor binders are required, resulting in a simplified AE architecture that reduces weight, thickness, and imparts flexibility and printability to the electrodes. SWNTs consisting of rolled graphene sheets built from sp^2-hybridized carbon atoms have attained immense attention due to their fascinating physicochemical properties including high aspect ratio, high active surface area, and exceptional electrical and mechanical properties. SWNTs possess higher electrical conductivity (~10^2–10^4 S cm^{-1}) than activated carbon (0.1–1 Scm^{-1}) [12]. Huang et al. studied electrocatalyst of oxygen reduction reaction of Pt supported on SWNTs (along with carbon and binder) support as a gas diffusion electrode [13]. Our group earlier reported such a promising approach based on the surfaces of additive-free and densely packed silver nanoparticles decorated P3-SWNTs entangled network to fabricate AEs, where, size-dependent catalytic activity of silver on SWNTs was found to accelerate oxygen reduction reaction [14]. Based on further investigations, in this research paper, we report fabrication of paper-like free-standing hybrid layer of highly conducting SWNTs flexible air electrode architecture via a simple vacuum filtration process.

Thus, the aforesaid properties have been achieved by tailoring hybrid $AE_{(P2/P3)}$ layer of non-functionalized (P2)- and functionalized (P3)-SWNTs. The P2-SWNTs in such AEs avoid electrolyte flooding within the pores, thus allowing free O_2/air diffusion while P3-SWNTs offers an advantage of good wet ability with electrolyte and blocks the gas flow for preventing zinc anode contamination. Electrochemical properties of such P2- and P3-SWNTs-based AE employed in zinc–air batteries have been investigated, and it is observed that such $AE_{(P2/P3)}$ delivers improved electrochemical properties as compared to conventional carbon-based AEs. Uniform morphology, high porosity, conductivity, and mechanically integrity of $AE_{(P2/P3)}$ opens attractive possibilities in future metal–air systems including Li–air batteries.

Experimental

Electrode preparation

Hybrid layer $AE_{(P2/P3)}$ with varying compositions (weight percent) of P2- and P3-SWNTs (Carbon Solutions, Inc., Riverside, CA) were prepared via a simple vacuum filtration process using homogeneous suspensions of SWNTs. For suspension I, SWNTs functionalized with carboxylic groups (P3) and for suspension II, the purified SWNTs (P2) have been used. In both cases, the SWNTs were dispersed (0.5 mg ml^{-1}) in deionized water containing 1 wt.% surfactant (sodium dodecyl sulfate, Alfa Aesar®) followed by ultrasonication (120 kW) for 30 min. To prepare the bucky paper, the suspensions of P3-SWNTs were filtered followed by P2-SWNTs through a membrane (Whatman, Anodisc alumina filter membranes; pore size, 20 nm) using a filter flask equipped with the vacuum pump. The resultant layer of P2-SWNTs was thoroughly washed with deionized water until there were no traces of surfactant. The deposited SWNTs' hybrid layer was dried overnight in a dry box at 60 °C under vacuum. Paper-like free-standing SWNTs membranes (~80 μm) with an average thickness of P2-SWNTs (~30-60 μm) layer and P3-SWNTs (~20–50 μm) layer was peeled off from the filter and employed as $AE_{(P2/P3)}$ without any further treatment. The zinc anode was prepared by mixing zinc powder (Alfa Aesar) with polyvinylidene fluoride binder taken in the ratio 80:20 by weight. The components were mixed as viscous slurry in *N*-methyl pyrrolidone solvent to get uniform mixture and heated for 4 h at 85±2 °C under vacuum. The resultant paste was coated on Al foil by doctor blade and then roller-pressed into a thickness of 50 μm, and the area of the negative electrode was 2 cm^2.

A schematic representation of zinc–air batteries employing proposed flexible architecture using $AE_{(P2/P3)}$ compared with the conventional architecture is elucidated in Fig. 1. A conventional zinc–air battery is shown in Fig. 1a and c consisting of a zinc foil and multilayered carbon with PTFE binder pressed (few microns thick) onto the nickel mesh as the air electrode. In contrast, a zinc–air cell design adopted in the present work is shown in Fig 1b and d which consists of a zinc anode and a paper-like free-standing thin hybrid air electrode without any binder consisting of hydrophobic (P2) and hydrophilic (P3)-SWNTs in varying compositions, thus resulting in a simplified, flexible, and printable zinc–air battery configuration.

Materials characterization

Surface morphology of the $AE_{(P2/P3)}$ was observed by field emission scanning electron microscopy (Jeol JSM7600F) after gold sputtering. Thermal properties were evaluated by thermogravimetric analysis (TGA, SDT-Q500 TA Instruments) at a heating rate of 10 °C min^{-1} from 30 to 900 °C under air atmosphere. Fourier transform infrared spectroscopy (FTIR) was performed (Perkin-Elmer GX FTIR) to identify the P3-SWNTs functionalization (−COOH group). Wetting properties due to P2 and P3-SWNTs compositions

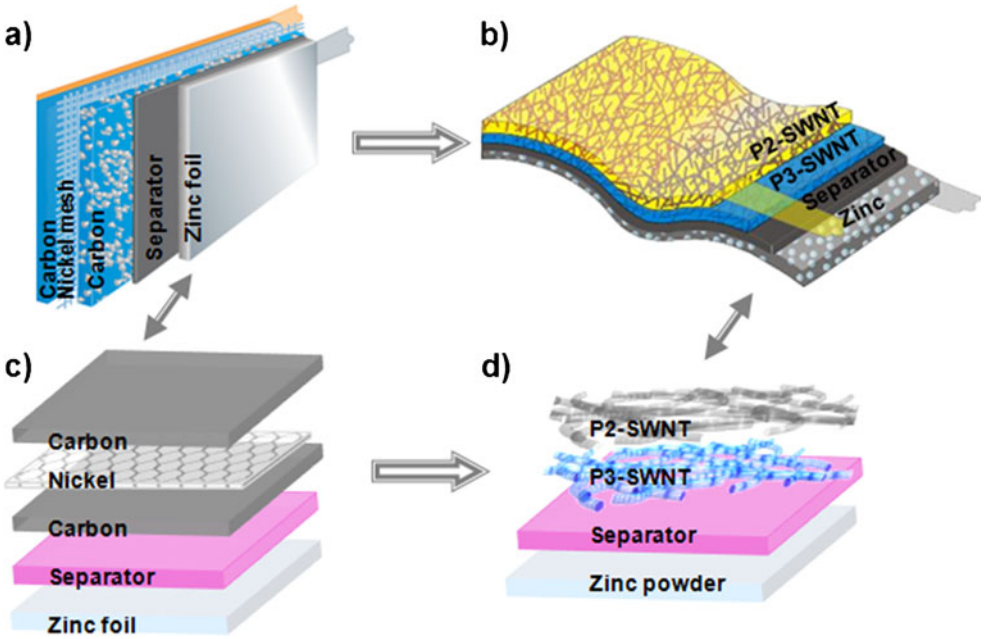

Fig. 1 Schematic representation of **a** and **c** conventional zinc–air batteries employing multilayered carbon and zinc foil and **b** and **d** flexible zinc–air batteries architecture using P2/P3-SWNT-based paper-like free-standing hybrid air electrode and zinc anode

in the hybrid $AE_{(P2/P3)}$ were studied by contact angle measurements (FTA 200 Dynamic Contact Angle Analyzer) using Sessile drop method in air. The adsorption of electrolyte (6 M KOH) solution by hybrid $AE_{(P2/P3)}$ was also measured to evaluate the wettability. Samples of $AE_{(P2/P3)}$ were soaked in an electrolyte solution and exposed to air at room temperature for 3 h. The adsorption is determined from the weight gain of the air electrode $AE_{(P2/P3)}$.

A NOVA Station[@] e series 3200 (Quantachorme Instruments) instrument was used to measure the nitrogen adsorption–desorption isotherms at 77.3 K in the range of absolute pressures (P/P_0) from 10^{-6} to 1. The samples were degassed at 200 °C under vacuum for 2 h prior to each analysis. The porosity (P) was determined by immersing the dry electrodes in *n*-butanol for 1 h [15]. The following relation was used to calculate P:

$$P(\%) = \frac{M_{\mathrm{BuOH}}/\rho_{\mathrm{BuOH}}}{M_{\mathrm{BuOH}}/\rho_{\mathrm{BuOH}} + M_{\mathrm{m}}/\rho_{\mathrm{P}}} \times 100$$

where, M_{m} is the mass of the dry electrode membrane, M_{BuOH} is the mass of *n*-butanol absorbed, ρ_{BuOH} and ρ_{P} are the densities of *n*-butanol (0.81 $\mathrm{gcm^{-3}}$) and SWNTs (2.1 $\mathrm{gcm^{-3}}$) (density obtained from supplier database), respectively.

In order to characterize the mechanical properties of $AE_{(P2/P3)}$ air electrode in ambient environment, test specimens of rectangular cross-sections (4.2-mm wide and 6.58-mm long) and thickness ~44 μm were tested under tension without further modification. Static mechanical uniaxial in-plane tensile tests were conducted with a dynamic mechanical analyzer (PerkinElmer® DMA Q800, TA Instruments). Sample width and thickness was measured using standard calipers (Mitutoyo). The length between the clamps was measured by the DMA instrument. The samples were gripped using film tension clamps with a clamp compliance of about 0.57 μm N^{-1}. The tensile and dynamic mechanical properties of the SWNTs-based air electrode $AE_{(P2/P3)}$ at a strain rate of 0.48%$\mathrm{min^{-1}}$ were conducted.

Cell fabrication and testing

Prototype zinc–air batteries were assembled in our laboratory by stacking zinc anode pressed on the Al foil (~2 $\mathrm{cm^2}$), Celgard 2400 polypropylene (PP, Celgard. LLC, Charlotte, NC), hybrid layer of $AE_{(P2/P3)}$, a Ni wire (~0.5 mm in diameter) as the current collector, and air access holes drilled on the positive side (viz., AEs) into a coin cell cap. To activate the cell, 200 μL of 6 M potassium hydroxide (KOH) aqueous solution was added as an electrolyte. The zinc anode was protected by the proper sealing of the coin cell. Ionic conductivity of the full zinc–air cell was measured by an AC impedance method using a frequency analyzer (Solartron 1260, London Scientific) at room temperature. The measurements were performed in the frequency range of 100 mHz to 1 MHz at an amplitude of 20 mV. Electrochemical properties were evaluated using a charge–discharge unit (AFBPI, Pine Instruments Co., Grove City, PA) at a constant current of 1 mA in a voltage range between 0 and 1.3 V at room temperature.

Results and discussion

Morphological characterization of $AE_{(P2/P3)}$

FE-SEM micrographs of P2- and P3-SWNTs-based $AE_{(P2/P3)}$ prepared by vacuum filtration method (Fig. 2) showed

uniform surface morphology, and the interlaying of SWNTs formed a three-dimensional network structure with fully interconnected macropores and multifibrous layers. The diameter of the P2-SWNTs bundles (~50–60 nm) was twice as large as those of these P3-SWNTs (~20–30 nm). The porous network resulted from the loose packing of CNTs in the hybrid layers of the air electrode. The zigzag interlaying of the CNTs imparts better mechanical strength for easy handling and flexible design. Scanning electron micrographs revealed significant differences between the morphology of P2 and P3 surfaces (Fig. 2) in the hybrid air electrode, owing to several factors, including differences in nanotube dimension, defect density, and degree of impurities in bundled nanotubes. Elena Bekyarova et al. have also reported a similar morphology [16]. The bundled morphology of P3-SWNTs was rather dense and smooth as compared to P2-SWNTs, due to the high purity achieved for the former by acid treatment. P3-SWNTs had relatively lower bundle diameter (bundle thinning) owing to the increase in Van der Waals forces between the P3-SWNTs that lead to compact binding between the individual nanotubes. The larger bundle diameter of P2-SWNTs allows controlled diffusion of the O_2/air due to the smaller pores in the network. On the contrary, relatively smaller bundle diameter of the P3-SWNTs makes it possible to distribute the nanotubes more uniformly in the electrode and to introduce a high surface area to come in contact with the electrolyte. Hybrid $AE_{(P2/P3)}$ takes advantage of characteristic properties of both P2- and P3-SWNTs, to yield a simplified and flexible electrode architecture for metal–air systems.

Thermal and structural characterization of $AE_{(P2/P3)}$

Thermogravimetric analysis (TGA) was performed on both P2- and P3-SWNTs under air atmosphere and thermograms are displayed in Fig. 3. Significant differences in thermal stability have been observed between P2- and P3-SWNTs, which can be attributed to the degree of functionalization. The initial weight loss observed ~50 °C is due to the evaporation of water molecules. P2-SWNTs appear to be stable up to 500 °C, followed by a sharp continuous drop indicating single degradation for P3-SWNTs, viz., first step from 55 to 379 °C (25%) and second step from 379 to 670 °C (70%). At 500 °C, the weight loss of about 5% is observed for P2-SWNTs, while for P3-SWNTs, the weight loss is about 70%. The char yield at 800 °C is estimated about 8.5% for both the samples. In the case of P3-SWNTs, the observed decomposition is a completed step degradation, which starts at 55 °C and showed weight loss of 10% at 85 °C. In comparison with P2-SWNTs, there is a two-step sharp at ~680 °C. The lower thermal stability of P3-SWNTs as compared to P2-SWNTs is attributed to the presence of carboxylic groups [17].

In order to confirm the presence of carboxylic functional groups in the P3-SWNTs, FTIR analysis was performed, and the spectrum is shown in Fig. 4. The absorption peaks present at 1,700–1,735 cm^{-1} are associated with the symmetric and asymmetric C = O stretching of the carboxylic acid (−COOH) group [18]. The broad absorption bands at 3,500 cm^{-1} are attributed to the hydroxyl (−OH) group. This might have resulted due to water [19] and –OH functional groups resulting from the chemical treatment during the purification and functionalization process [20, 21]. Absorption peaks present at 1,600 cm^{-1} corresponds to C = C bond stretching vibration of the CNTs [22]. A significant absorption occurred at around 1,550 cm^{-1}, may be attributed to carboxylate anion stretching vibration [23]. Thus, the generation of –OH and –COOH groups due to functionalization of P3-SWNTs is observed.

$AE_{(P2/P3)}$ physical properties and contact angle measurements

The hybrid $AE_{(P2/P3)}$ bucky paper fabricated have an aesthetic appearance of a smooth black surface (thickness, ~80 μm). They are paper-like free-standing membranes with the porosity of 70% and mechanically robust upon bending and abrasion. The good mechanical strength is due to the cobweb network formed by P2- and P3-SWNTs. The electrical conductivity of hybrid $AE_{(P2/P3)}$ bucky paper was measured to be 1×10^3 S cm^{-1} at room temperature. The wetting properties of the hybrid $AE_{(P2/P3)}$ bucky paper SWNTs electrode were investigated by measuring the contact angle with 6 M KOH electrolyte at both P2 and P3 sides of the hybrid $AE_{(P2/P3)}$ bucky paper. The plot of contact angle and wetting properties depending on the surface nature of AEs with different proportions of P2- and P3-SWNTs is shown in Fig. 5. The contact angle of AE made up of P3-SWNTs alone $AE_{(P3)}$ showed total wetting with contact angle of almost 0° (Fig. 5a) whilst that of P2-SWNT $AE_{(P2)}$ was 123° (Fig. 5c) indicating the hydrophilic nature of the former and relatively hydrophobic nature of the latter. The contact angle measured on both sides of the hybrid $AE_{(P2/P3)}$ bucky paper is observed to increase with increasing P2-SWNTs content (Fig. 5b). In the case of the P2 side (hydrophobic) of $AE_{(P2/P3)}$, the contact angle values are 0°, 94.6°, and 123° for the P2 content of 0, 50, and 100 wt.%, respectively. The contact angle of the P3 side is 38.5° for the P2 content of 50 wt.%, which is ~60% less than that observed from P2 side (Fig. 5d). This demonstrates the improved hydrophobic nature of $AE_{(P2/P3)}$ with decreasing weight percent of P3-SWNTs. It is worth noticing that the carboxyl functionalized SWNTs have the lowest contact angles 0° at the highest weight percent and the highest contact angle 123° at the lowest weight percent, evidence of easier infiltration by the P2-SWNTs into the

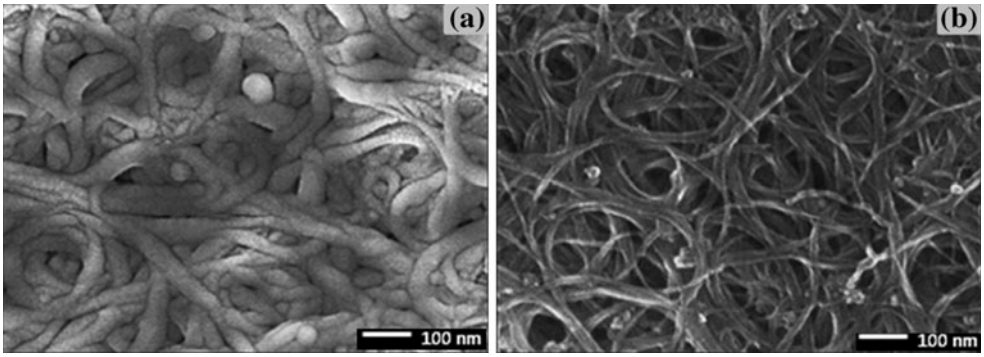

Fig. 2 Field emission scanning electron micrographs of images of the free-standing bucky paper, sides **a** P2-SWNTs and **b** P3-SWNTs showing surface morphology of hybrid air electrode

P3-SWNTs at a specific optimized composition of hybrid $AE_{(60/40)}$.

The electrolyte (6 M KOH) adsorption on the hybrid $AE_{(P2/P3)}$ bucky paper revealed the significant weight gain after 3 h. The wettabilty due to electrolyte absorption of the $AE_{(40/60)}$, $AE_{(60/40)}$, and $AE_{(80/20)}$ is observed to be 107.64, 96.66, and 34.76 $mm^3\ g^{-1}$, respectively. The absorption characteristics are found dependent on the surface morphologies of the P2- and P3-SWNTs, i.e. difference in their diameters and spacing between each CNTs. The functionalised P3-SWNTs in the hybrid $AE_{(P2/P3)}$ bucky paper produces a large amount of air trapped between the nanostructure of the CNTs and are found more wettable by electrolyte solution than the other air electrodes. Also, hybrid $AE_{(P2/P3)}$ bucky paper has many nano-sized pores and comprised of hollow tubular structure CNTs, so the P3 side of the hybrid layer is much easily penetrated by electrolyte solution under the action of capillarity.

Typical nitrogen adsorption/desorption isotherms and the corresponding pore size distribution of $AE_{(60/40)}$ and $AE_{(80/20)}$ are recorded and shown in Fig. 6. Both the samples exhibit a type IV adsorption isotherm according to the IUPAC classification [24], with a condensation step as the relative pressure approaches unity. At low and intermediate relative pressures, an increase in nitrogen uptake suggests the presence of micropores in both the samples and further increase at high relative pressures, accompanied by hysteresis, indicative of capillary condensation within mesopores. Specific surface areas, calculated according to the Brunauer, Emmett, and Teller (BET) equation indicates the influence with the different content of P2- and P3-SWNTs in the hybrid air electrodes. The surface area recorded for $AE_{(80/20)}$ is slightly greater than that of $AE_{(60/40)}$. Typical values of BET surface areas for $AE_{(60/40)}$ are around 130.54 $m^2\ g^{-1}$, whereas for $AE_{(80/20)}$ are around 156.76 $m^2\ g^{-1}$, depending on the several, intertwined factors including purity, surface functionality, density of surface groups, and the state of aggregation of the P2- and P3-SWNTs. In the case of $AE_{(60/40)}$, the surface area is lower probably due to less COOH bonding on the P2 surface. COOH group attached (branching out from the tubes) on the SWNTs inevitably increase the surface area. Thus, the lesser content of P3-SWNTs leads to relatively lower surface area. The pore size distributions, obtained from the Barret, Joyner, and Halenda (BJH) method, are given in the inset of Fig. 6. Both the samples present only a major peak in the pore size distribution, indicating that majority of the pore size are less than 15 nm. Thus, the increase in the P2-SWNTs content in the hybrid air electrode matrix limits the accessibility of the smaller pores, which also results in the decrease of the BET-specific surface area.

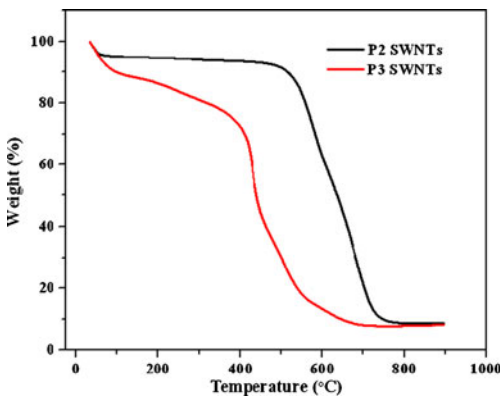

Fig. 3 TGA of P2- and P3-SWNTs under ambient atmosphere (30 to 900 °C, 10 °C/min) for evaluating the change in thermal behavior of P2-SWNTs after functionalization

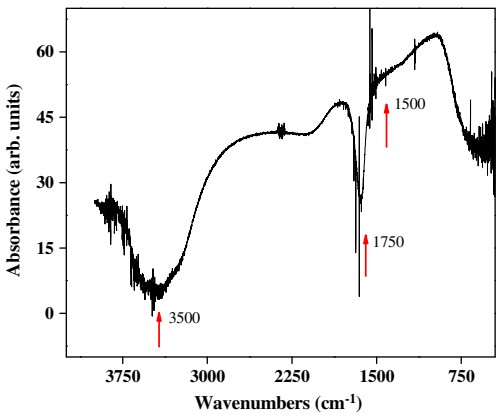

Fig. 4 FTIR Spectra of P3-SWNTs for confirming the presence of functional groups on P3-SWNTs

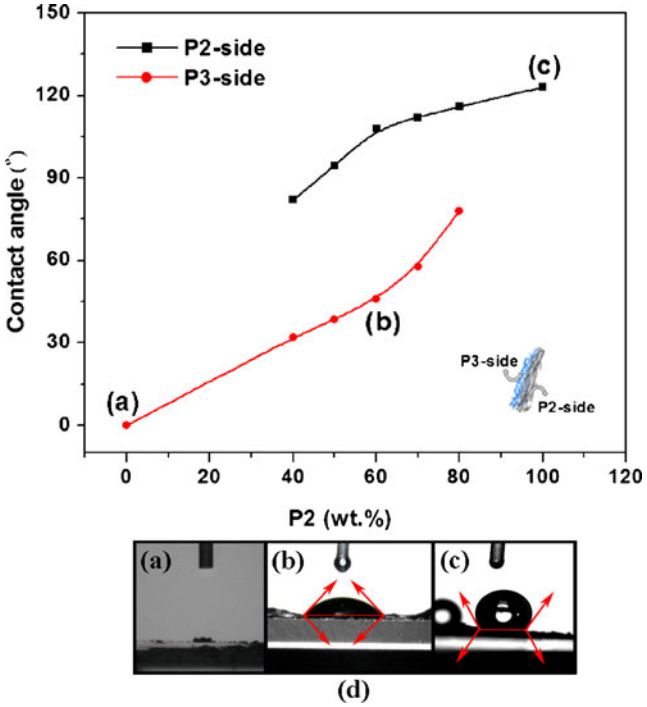

Fig. 5 Contact angle of the air electrode **a** $AE_{(P3)}$, **b** $AE_{(P2/P3)}$ (hydrophilic P3 side), **c** $AE_{(P2)}$, and **d** variation of contact angle with different (P2/P3) content (compositions *a*, *b*, and *c* are marked on the graph)

Typical stress–strain curves, from which, the effective elastic modulus and the tensile strength of the specific optimized composition of hybrid $AE_{(60/40)}$ were obtained, are shown in Fig. 7. Tensile test measurements of $AE_{(60/40)}$ revealed high values of tensile modulus and fracture strength and have shown good dimensional stability. The ultimate tensile strain for the air electrode $AE_{(60/40)}$ is observed to be 0.61%. The mechanical strength results in high tensile strength and high elastic modulus. The average modulus of $AE_{(60/40)}$ was determined to be 2.24 GPa and fracture strength ~11.53 MPa, in good agreement with experimental findings of the modulus of bucky paper [25]. The mechanical strength parameters for hybrid $AE_{(80/20)}$ have indicated almost similar tensile characteristics. These mechanical properties such as breaking strain and breaking stress of macroscopic assembly of SWNTs such as bucky paper are mainly induced from the interaction between functionalized and non-functionalized SWNTs, and the supporting forces are Van der Waals force and/or entanglement of SWNTs. Thus, the mechanical properties of SWNT-based air electrodes are mainly dominated by the nature and strength of the junctions between individual nanotubes as already reported by P.G. Whitten et al. [26] and may serve as the basis for future high-strength metal–air battery designs.

Thus, ionic conductivity, interfacial resistance, and discharge characteristics of the zinc–air cell with optimized

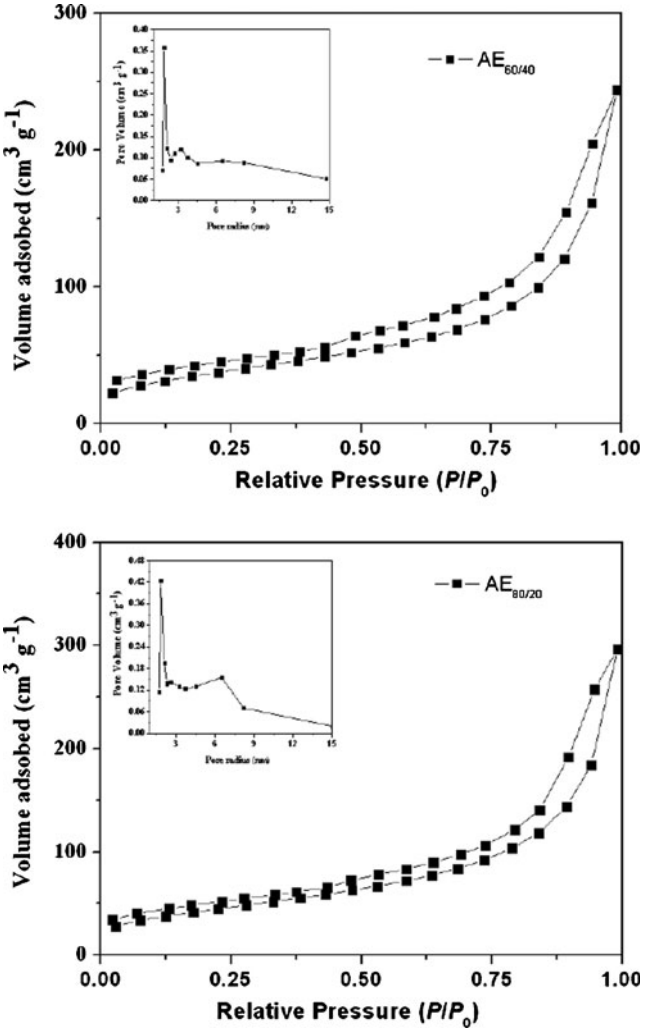

Fig. 6 N_2 adsorption–desorption isotherm of $AE_{(60/40)}$ and $AE_{(80/20)}$ (*inset*: the corresponding pore size distribution obtained from adsorption branch calculated by BJH method)

composition of hybrid $AE_{(60/40)}$ are measured and compared with the performance of $AE_{(80/20)}$ electrodes.

Ionic conductivity and interfacial resistance of cell

The ionic conductivity of the zinc–air cell was measured by AC impedance method. The impedance spectrums observed with the different compositions of P2- and P3-SWNTs at room temperature are presented in Fig. 8. The bulk resistance values for the cells with $AE_{(60/40)}$ and $AE_{(80/20)}$ compositions are 3.5 and 4.7Ω, respectively. From the impedance data, the ionic conductivity values are calculated as 1×10^{-2} and 7.2×10^{-3} S cm^{-1} for $AE_{(60/40)}$ and $AE_{(80/20)}$, respectively. From the results, it is clear that the cell conductivity is higher for the increased P3-SWNTs content. This can be attributed to the enhanced conducting channels due to the increasing hydrophilic/smooth surface nature of bucky paper achieved with higher P3-SWNTs content.

The Nyquist plots obtained from the electrochemical impedance spectra for a Zn–air cell with hybrid air electrodes $AE_{(60/40)}$ (time dependent) and $AE_{(80/20)}$ are shown in Fig. 8. As clearly seen, a depressed semicircle in the high to low frequency range is observed for both the cells. A nonlinear least-square fit program was utilized to interpret the impedance spectra in terms of the equivalent circuit shown in the inset of Fig. 9. The intercept towards the real axis in the high frequency end represents the electrolyte resistance, which is the major contribution towards the total resistance from the bulk resistance (R_b) and only minor contribution of the grain boundary resistance. The value of R_b is observed to be very low (3.5–7 Ω). There is no appreciable increase in R_b with storage time. This behavior is indicative of a good retention of the ionic conductivity and good performance of the cell. The observed semicircles are typical of air electrode/electrolyte interfacial resistance (R_f). The interfacial resistance (R_f) of the cell is mainly estimated by the compatibility of the electrolyte with an air cathode. A constant phase element is considered in place of the capacitance corresponding to the capacitance at the porous air electrode surface. In addition, the finite length Warburg resistance, represented by Z_w, was utilized to evaluate a diffusion-controlled process.

The interfacial resistance of the cell having the $AE_{(60/40)}$ and $AE_{(80/20)}$ is shown in Fig. 9. The initial R_f value of the cell having the $AE_{(60/40)}$ is 220 Ω. The interfacial resistance is initially quite low and increases slowly upon storage time and observed to increase to 380 Ω after 1 day. In the case of $AE_{(80/20)}$, the initial R_f is 580 Ω, which is much higher as compared to cells with $AE_{(60/40)}$. The increase in R_f with time is expected in metal–air batteries indicating the formation and growth of the solid electrolyte interface (SEI) layer on the metal surface by reaction with the electrolyte components, impeding the passage of ions. The formation of SEI layer prevents further reaction of the electrolyte with zinc anode, helps to enhance the cathodic limit of the electrolyte, and thus improves battery performance. These favorable interfacial properties reflect a good air electrode behavior with electrolyte making it very promising candidate for safe, reliable, and long-lasting zinc–air batteries.

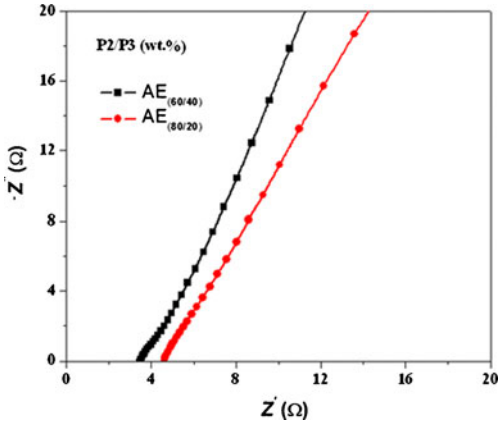

Fig. 8 Evaluation of conductivity using AC impedance spectra of zinc–air cell with $AE_{(60/40)}$ and $AE_{(80/20)}$ (frequency range, 100 mHz to 1 MHz, 20 mV, 25 °C)

Discharge properties of $AE_{(P2/P3)}$ in zinc–air batteries

The hybrid layer $AE_{(P2/P3)}$ electrodes have been evaluated for discharge performance in zinc–air battery at room temperature. The discharge properties are compared for different P2- and P3-SWNT compositions and are shown in Fig. 10. Relatively high cathode utilization was achieved for the cells with $AE_{(P2/P3)}$ having higher P2-SWNTs. The observed differences in the discharge capacity can be attributed to compositional differences of P2- and P3-SWNTs. The cell having $AE_{(60/40)}$ delivers a capacity 300 mAh g^{-1}, which is 8–24% higher than other $AE_{(P2/P3)}$ combinations. The difference in capacity may probably be due to the difference in utilization of active material, depending on the thickness of the hydrophobic (P2) and

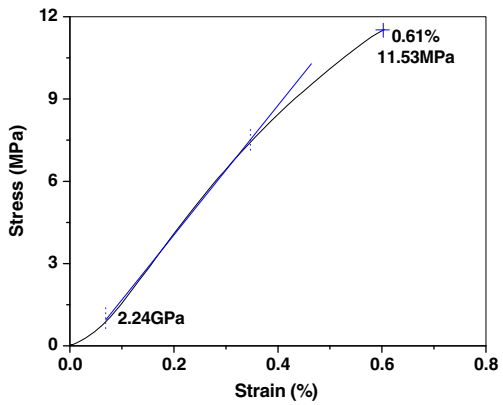

Fig. 7 Tensile test result for dry air electrode $AE_{(60/40)}$

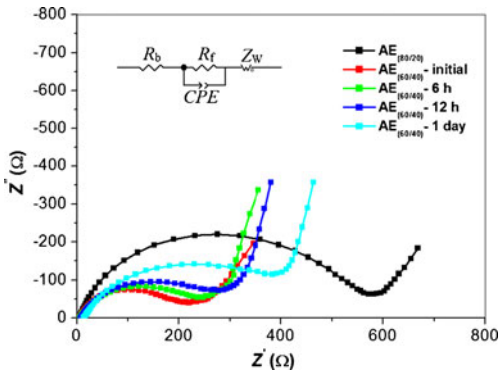

Fig. 9 Impedance of zinc–air cell with $AE_{(60/40)}$ (time dependent) and $AE_{(80/20)}$ (100 mHz to 1 MHz, 20 mV), the equivalent circuit is shown in the *inset*

hydrophilic (P3) layers of AE. It is observed that the discharge capacity increases with the hydrophobic (P2) content to the maximum and then starts to decrease. Among the cells based on $AE_{(60/40)}$ shows the highest discharge capacity (>8%) on bare SWNTs. This can be explained by an optimum point of improved three-phase interface generated between electrolyte, electrode, and O_2/air. The discharge capacity of cells is observed to decrease with further increase of P2-SWNT content (>60 wt.%). This can be explained by the higher thickness of the hydrophobic layer in $AE_{(P2/P3)}$, will decrease the availability of zinc anions due to the poor ion conduction path. The hydrophobic nature of P2-SWNTs may block the electrolyte, which leads to control the mobility of zinc ions beyond the optimum ratio of $AE_{(60/40)}$. The difference in ionic conductivity also may affect the discharge property. It is found in well agreement with the observed R_b values for the cells having $AE_{(60/40)}$ and $AE_{(80/20)}$ compositions as explained in the section "Ionic conductivity and interfacial resistance of cell". The good discharge capacity of the cell can be attributed to enabling free passage of ions between the electrode and good compatibility between the electrolyte and electrodes. This evaluation demonstrates the advantages of $AE_{(P2/P3)}$ for zinc–air batteries.

Cells based on $AE_{(60/40)}$ composition were discharged at different current densities, 0.25, 1.0, and 1.5 mA. It is seen that the discharge capacity decreasing with increasing the discharge current as shown in Fig. 11. A discharge capacity of 375 mAh g^{-1} is obtained at a discharge current 0.25 mA. The discharge capacity is decreased to 238 mAh g^{-1} at a discharge current 1.5 mA. Although, it is observed that there is no considerable voltage drop with different discharge currents. The characteristic of extremely flat cell reaction voltage of the cell reveals the good kinetics of redox reaction at all tested current densities. With an increase in current density, polarization is enhanced due to slow zinc ion diffusion at the solid, two-phase ZnO/Zn $(OH)_2$ interface and the resulting limitation of the material to cope with the fast reaction kinetics at high current rates. Further improvement in the present air electrode architectures is underway in terms of catalyst addition to further develop such binder-free flexible hybrid air electrode architectures that can exhibit comparable performance with present commercial zinc–air batteries at higher current rates and loads.

Conclusion

Compared with the conventional multilayered carbon-based air electrodes mixed with PTFE binder, paper-like lightweight, binder-free, and flexible architecture of hydrophobic (P2) and hydrophilic (P3)-SWNT-based $AE_{(P2/P3)}$ were

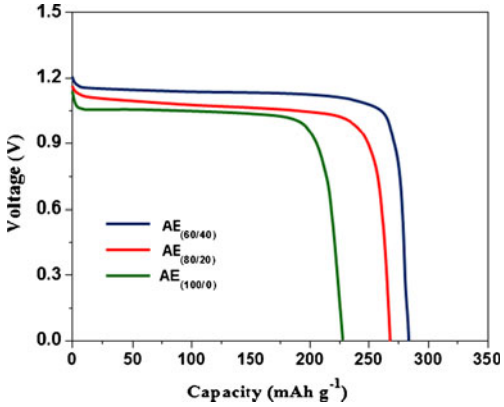

Fig. 10 Discharge capacity of zinc–air cell with $AE_{(60/40)}$, $AE_{(80/20)}$, and $AE_{(100)}$ (25 °C, 1 mA, 0–1.3 V)

prepared and evaluated for zinc–air batteries. Surface characterization by FE-SEM reveals uniform morphology with fully interconnected pore structure in AEs. High porosity (~70%) achieved in bucky paper leads to room temperature ionic conductivity (~1×10^{-2} S cm^{-1}) for zinc–air cell. The formation of the passivation layer of ZnO was evaluated by AC impedance and is found that there is a considerable increase in interfacial resistance with storage time. The cell assembled with bucky paper having $AE_{(60/40)}$ delivers a discharge capacity of ~300 mAh g^{-1} at a current density of 1 mA. By exploiting the benefits of P2- and P3-SWNTs in $AE_{(P2/P3)}$, a relatively higher discharge capacity is observed for bare P3-SWNT in combination with optimized P2-SWNTs (<60 wt.%), opening possibility for future battery applications. In this optimum range $AE_{(P2/P3)}$ shows high active surface area ~130.54–158.76 m^2 g^{-1} to facilitate oxygen reduction/evolution in zinc–air cells. The unique physical, mechanical, and electrochemical properties of P2- and P3-SWNT-based paper-like free-standing hybrid $AE_{(P2/P3)}$ makes it a promising candidate in zinc–air batteries and elaborate their use as AEs in future lithium–air batteries too.

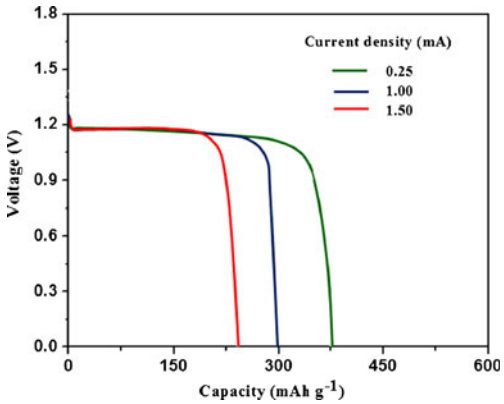

Fig. 11 Discharge capacity of zinc–air cell with $AE_{(60/40)}$ at different current densities **a** 0.25 mA, **b** 1.0 mA, and **c** 1.5 mA (25 °C)

References

1. Deiss E, Holzer F, Haas O (2002) Modeling of an electrically rechargeable alkaline Zn-air battery. Electrochim Acta 47:3995–4010
2. Goldstein J, Brown I, Koretz B (1999) New developments in the Electric Fuel Ltd. zinc air system. J Power Sources 80:171–179
3. Chkkaravarthy C, Waheed AKA, Udupa HVK (1981) Zinc-air alkaline batteries—A review. J Power Sources 6:203–228
4. Mohamad AA (2006) Zn/gelled 6M KOH/O_2 zinc–air battery. J Power Sources 159:752–757
5. Bidault F, Brett DJL, Middleton PH, Brandon NP (2009) Review of gas diffusion cathodes for alkaline fuel cells. J Power Sources 187:39–48
6. Han JJ, Li N, Zhang TY (2009) Ag/C nanoparticles as an cathode catalyst for a zinc-air battery with a flowing alkaline electrolyte. J Power Sources 193:885–889
7. Lee CW, Sathiyanarayanan K, Eom SW, Kim HS, Yun MS (2006) Effect of additives on the electrochemical behaviour of zinc anodes for zinc/air fuel cells. J Power Sources 160:161–164
8. Bender SF, Cretzmeyer JW, Reise TF (2002) Zinc/air batteries—button configuration. In: Linden D, Reddy TB (eds) Handbook of batteries, 3rd Eds. McGraw-Hill, New York, p 13.1
9. Neburchilov V, Wang H, Martin JJ, Qu W (2010) A review on air cathodes for zinc–air fuel cells. J Power Sources 195:1271–1291
10. Kortesch K, Simander G (1996) Fuel Cells. VCH, Weinheim, Germany
11. Hamann CH, Vielstich W, Hamnett A (1998) Electrochemistry. Wiley-VCH, Weinheim, Germany
12. Landi BJ, Ganter MJ, Cress CD, DiLeo RA, Raffaelle RP (2009) Carbon nanotubes for lithium ion batteries. Energy Environ Sci 2:638–654
13. Huang H, Zhang W, Li M, Gan Y, Chen J, Kuang Y (2005) Carbon nanotubes as a secondary support of a catalyst layer in a gas diffusion electrode for metal air batteries. J Colloid Interface Sci 284:593–599
14. Wang T, Kaempgen M, Nopphawan P, Wee G, Mhaisalkar S, Srinivasan M (2010) Silver nanoparticle-decorated carbon nanotubes as bifunctional gasdiffusionelectrodes for zinc–air batteries. J Power Sources 195:4350–4355
15. Raghavan P, Zhao X, Kim JK, Manuel J, Chauhan GS, Ahn JH, Nah C (2008) Ionic conductivity and electrochemical properties of nanocomposite polymer electrolytes based on electrospun poly (vinylidenefluoride-co-hexafluoropropylene) with nanosized ceramic fillers. Electrochim Acta 54:228–234
16. Bekyarova E, Itkis ME, Cabrera N, Zhao B, Yu A, Gao J, Haddon RC (2005) Electronic properties of single-walled carbon nanotube networks. J Am Chem Soc 127:5990–5995
17. Hu H, Ni YC, Mandal SK, Montana V, Zhao N, Haddon RC, Parpura V (2005) Enhancement of adsorption inside of single-walled nanotubes:opening the entry ports. J Phys Chem B 109:4285–4289
18. Kuznetsova A, Mawhinney DB, Naumenko V, Yates JrJT, Liu J, Smalley RE (2000) Polyethyleneimine functionalized single-walled carbon nanotubes as a substrate for neuronal growth. Chem Phys Lett 321:292–296
19. Holzinger M, Vostrovsky O, Hirsch A, Hennrich F, Kappes M, Weis R, Jellen F (2001) Sidewall functionalization of carbon nanotubes. Angew Chem Int Engl Ed 40:4002–4005
20. Kovtyukhova NI, Mallouk TE, Pan L, Dickey EC (2003) Individual singlewalled nanotubes and hydrogels made by oxidative exfoliation of carbon nanotube ropes. J Am Chem Soc 125:9761–9769
21. Colthup NB, Daly LH, Wiberlay SE (1990) Introduction to infrared and Raman spectroscopy. Academic Press, Boston
22. Saito R, Dresselhaus G, Dresselhaus MS (1999) Physical properties of carbon nanotubes. Imperial College Press, London, 183
23. He B, Sun W, Wang M, Liu S, Shen Z (2004) Preparation and characterization of a series of novel complexes by single-walled carbon nanotubes (SWNTs) connected poly(amicacid) containing bithiazole ring. Mater Chem Phys 84:140–145
24. Gregg SJ, Sing KSW (1982) Adsorption, surface area and porosity. Academic Press, New York, 154
25. Zhang X, Sreekumar TV, Liu T, Kumar S (2004) Properties and structure of nitric acid oxidized single wall carbon nanotube films. J Phys Chem B 108:16435–16440
26. Whitten PG, Spinks GM, Wallace GG, (2005) Mechanical properties of carbon nanotube paper in ionic liquid and aqueous electrolytes. Carbon 43:1891–1896